GEOMETRIC HORIZONS IN THE SZEKERES SPACETIME

by

Nicholas Layden

Submitted in partial fulfillment of the requirements
for the degree of Master of Science

at

Dalhousie University
Halifax, Nova Scotia
August 2020

Table of Contents

Abstract

A new conjecture for geometric horizons has been introduced which may provide a potential alternative to using apparent horizons and related surfaces for analyzing the dynamics of black hole spacetimes. In particular, using two examples of black hole formation in a collapsing universe in the Szekeres spacetime, the formation, evolution, and detection of geometric horizons are shown. In addition, a function for detecting apparent horizons in the Szekeres spacetime is also considered, and it is shown that the apparent horizon in the Szekeres model, is in fact, a geometric horizon. The Cartan-Karlhede algorithm for determining local equivalences of spacetimes is used to compute an invariant frame in the Newman Penrose frame formalism, and Cartan invariants derived from the spacetime in this frame are shown to detect the geometric horizons under various conditions on the curvature tensors of the spacetime. One model for primordial black hole formation and another for galactic black hole formation are considered with non-zero cosmological constants, generalizing work published previously on these models with zero cosmological constant. Future work utilizing geometric horizons may provide benefits in gravitational wave research involving black hole mergers.

Chapter 1

Introduction

1.1 General Relativity

The development of Einstein's general theory of relativity rests heavily on top of the framework of differential geometry and the language of tensor mechanics. The manifolds here are 4-dimensional Pseudo-Riemannian. Einstein's field equations (EFEs) have the form [10]

$$\mathrm{G}_{\mu\nu} + \Lambda \mathrm{g}_{\mu\nu} = \kappa \mathrm{T}_{\mu\nu}, \tag{1.1}$$

where $\mathrm{G}_{\mu\nu}$ is the Einstein tensor, which is characterized by the Ricci curvature tensor, the Ricci scalar and the spacetime metric. This term encodes all of the geometrical properties of the spacetime according to the metric.

$$\mathrm{G}_{\mu\nu} \equiv \mathrm{R}_{\mu\nu} - \frac{\mathrm{R}}{2}\mathrm{g}_{\mu\nu} \tag{1.2}$$

κ is a constant depending on the value of the speed of light c, the universal gravitation constant G, and the unit system used, defined by $\kappa = \frac{8\pi G}{c^2}$. Conventionally in relativity, the units are such that $c = G = 1$, so $\kappa = 8\pi$ is commonly used. The quantities $R_{\mu\nu}$ and R are the Ricci tensor and scalar respectively, which are the trace of the Riemann curvature tensor, and the trace of the Ricci tensor. The last term in (1.1), $\mathrm{T}_{\mu\nu}$ is the stress-energy tensor, and is where is encoded all of the physics of the models. This term essentially is the mass and energy term in the field equations.

The physical intuition for the equations here is that the properties of matter in the spacetime will induce a change in the manifold structure, which then responds by causing the matter and energy to move around the spacetime dynamically. Overall, the effect of gravitation is exactly this process of translating energy to curvature to motion.

Given a base assumption on the geometrical properties of a spacetime, the solution

to the field equations is a metric that describe all of the properties of the spacetime including the matter and energy. Solving the field equations for a particular metric allows us to model the dynamics of a physical system, and analyze properties of the solution within that framework, in our case it pertains to analyzing specific types of black hole dynamics.

1.1.1 Stress-Energy Tensor for a Perfect Fluid

The stress energy tensor for a perfect fluid can be given by [9]:

$$T_{\mu\nu} = (\rho + p)\, u_\mu u_\nu + p g_{\mu\nu} \tag{1.3}$$

where $\rho = \rho(x^\mu)$ is the energy density of the system, $p = p(x^\mu)$ is the pressure term, $g_{\mu\nu}$ is the metric of the spacetime, and u_μ is the comoving velocity on the manifold.

For some cases it is useful to set the pressure term to zero in the perfect fluid equation, resulting in the stress energy tensor for a pressureless dust field. In cosmology this makes sense on the largest scales of the universe where there is no effective pressure interaction between galaxies for example. The usefulness of a dust solution for black holes may not be fully compatible with a more realistic model, though analysis with dust solutions still remains a reasonable toy for the context of this work.

1.1.2 Coordinate Frame and Comoving Frame

A common coordinate frame used in relativity is the spherical coordinate system

$$e^\mu = \{dt, dr, d\theta, d\phi\} \tag{1.4}$$

For the stress energy tensor, u is taken to be a comoving timelike covector

$$u = u_\mu e^\mu = dt \tag{1.5}$$

This form for the covector was used to quantify the stress energy tensor for all examples. The Einstein summation convention on the indices in (1.5) is assumed for all future equations.

Szekeres Coordinate Frame

For the Szekeres models examined here, the coordinate frame used is a projective coordinate system, with a time component, a position coordinate, and two projective coordinates. The coordinate system is the projection mapping from spherical coordinates on each spherically symmetric shell. The coordinates have the form (t, z, x, y), where (x, y) are the projection coordinates, (t, z) are shell position coordinates. Each shell at position (t, z) is also spherically symmetric. A greater detailed analysis of the geometry of Szekeres models is given by Buckley [4].

1.1.3 Spacetime Metric

In GR, the type of metric used is Pseudo-Riemannian, and like Riemannian metrics, they define the line element operator on the space in an analogous way. This means that the signature of the metric diagonal elements is $\{-1, +1, +1, +1\}$ or $\{+1, -1, -1, -1\}$. The only rule for the signature is that the temporal and spatial terms in the diagonal will have opposite signs. The pseudo-Riemannian convention on the metric signature is what defines the notion of causality in the spacetime. Each spacetime metric is an exact solution to the EFEs, and fully characterizes all of the curvature properties of the spacetime, and other interesting things like where all the curvature singularities occur.

1.1.4 Example Spacetime Metrics

Schwarzschild

The Schwarzschild metric was the first exact solution to Einstein's equations, determined by Karl Schwarzschild in 1915, a short time before his death in 1916. The Schwarzschild metric given in its full form is: [22]

$$g = -\left(1 - \frac{2M}{r}\right) dt \otimes dt + \left(1 - \frac{2M}{r}\right)^{-1} dr \otimes dr + r^2 \left(d\theta \otimes d\theta + sin^2(\theta) d\phi \otimes d\phi\right) \tag{1.6}$$

where the units are such that $c = G = 1$, M is the gravitational mass of a point mass in the spacetime, and (r, θ, ϕ) are the standard spherical coordinates. This metric

describes a spacetime with a single point mass, is static, has spherical symmetry, and is asymptotically flat.

In this solution, we see that there are points in the metric where some terms become singular, at $r = 0$ and $r = 2M$. The interesting feature here is the surface defined by $r = 2M$, and what is now conventionally known as an event horizon for a Schwarzschild black hole [22].

Kerr

The Kerr metric is an exact solution to the field equations that is stationary, rotating and asymptotically flat. This type of model is one of the most common models used for simulating gravitational waves, as the end state of a black hole merger for example. The Kerr model is widely used in astronomy for characterizing accretion disks and X-ray emission from around supermassive black holes. Modern gravitational wave research also applies a lot of properties of the Kerr model in modelling the interactions between two or more black holes, and modelling gravitational wave emission from these systems.

Friedmann-Lemaître-Robertson-Walker

This metric is used for most modern forms of cosmology, and is built out of the initial assumptions of a spacetime that is spatially homogeneous and isotropic . The assumption of homogeneity in the universe is relaxed by the Szekeres model.

Szekeres

Generalized Szekeres models were developed to relax the spatial homogeneity condition in cosmological models [25]. There are two classes of Szekeres models, with a slightly different condition on the metric functions that change the behaviour of the solutions. The loss of homogeneity in the Szekeres models gives a much more reasonable, though much more complicated way to determine the cosmological dynamics of the universe, assuming that the universe is inhomogeneous on cosmological scales. It seems most relevant to compare Szekeres models to FLRW type cosmologies, where Szekeres models are a generalization of FLRW models.

1.1.5 Horizons

Einstein's field equations admit solutions in general that contain singularities. In fact this is a prominent feature of manifolds in general relativity [13]. Colloquially, certain types of singularities in spacetime solutions of Einstein's field equations are called black holes. Black holes are characterized by surfaces, typically called event horizons. There are a handful of types of horizons depending on what information you need to know about your system. The apparent horizon for a black hole is characterized by the surface for which the null expansion is zero, physically this means that its the surface where light is not falling into or radiating away.

Another way to characterize these objects conceptually, is by thinking of them physically as a subregion of space where the gravitational field is strong enough that even the motion of light out from that space on the horizon is not possible. The definition of a horizon in general depends on what property of the spacetime defines the surface. Apparent and event horizons are some of the different types of horizons, though are distinctly different types of objects.

1.1.6 General Types of Horizons

Event Horizon

The event horizon generally is thought of first when picturing the idea of what a black hole is supposed to be. This surface is defined as the boundary of the causal past of future null infinity. In other words, any signals sent from the interior of this region will never escape [2]. In general, to determine the location of event horizon, the global behaviour of the spacetime must be known (this means that the full time evolution of the universe must be determined!), and this idea of an event horizon presents a problem when we are trying to talk about black holes as local phenomena. We would like to propose alternative surfaces that are analogous to the event horizon in some way, yet are able to be determined locally, rather than globally.

Trapping Surfaces and Apparent Horizons

Starting with the idea of a trapping surface, a trapping surface is a closed two-surface that has the ingoing and outgoing null expansions are negative everywhere. Thus, for

a two-surface, with outgoing and ingoing directions ℓ^a and n^a:

$$\begin{aligned} \theta_{(\ell)} &\equiv q^{ab}\nabla_a \ell_b < 0 \\ \theta_{(n)} &\equiv q^{ab}\nabla_a n_b < 0, \end{aligned} \tag{1.7}$$

Where $q_{ab} = g_{ab} + 2\ell_{(a}n_{b)}$ is the projection operator of the metric restricted to the outermost trapping surface, typically called the marginally outer trapping surface (MOTS) [3].

A surface in the spacetime that is characterized by the outgoing null expansion vanishing ($\theta_{(\ell)} = 0$) is the MOTS. This idea of a trapping surface is also commonly called an apparent horizon in numerical relativity. If the spacetime can be foliated by asymptotically flat spacelike three-surfaces, then the boundary of these trapped surfaces is called the apparent horizon [12]. The apparent horizon is also defined by the foliation of the spacetime, and is not unique. Assuming we have a well defined vector for the outgoing null rays, the expansion of the null rays is zero at the MOTS. A surface foliated entirely by MOTS is referred to as a marginally outer trapped tube (MOTT) [3] . From here on, the apparent horizon will be explicitly defined apart from any other MOTS that appears.

Dynamical Horizons

The definition of a dynamical horizon [1, 3] is a smooth three-dimensional spacelike submanifold that is foliated by a preferred family of 2-surfaces such that on each 2-surface, the expansion of the outgoing null normal is zero, and the expansion of the ingoing null normal is strictly negative. So compared to the above definition of marginally trapped surfaces, a dynamical horizon is a manifold that is foliated by marginally trapped spatial 2-surfaces. Dynamical horions are also quasi-local objects like apparent horizons, and thus do not require full global knowledge of the spacetime.

Geometric Horizon

Due to the foliation dependent nature of the apparent horizon, it is important to determine another type of surface defined invariantly, such as the geometric horizon [6]. The geometric horizon is a hypersurface defined by the vanishing of certain Cartan invariants in the spacetime. For a spacetime with some algebraic type, the geometric

horizon is an invariant surface that is algebraically more special than the exterior spacetime. In a properly defined invariant frame, the existence of a geometric horizon can be determined by placing conditions on various scalar curvature invariants that define an algebraically special region [6, 5]. Having a way to invariantly characterize these surfaces allows us to describe special geometric surfaces analogous to the event horizons for stationary black hole solutions, or apparent horizons for dynamical black hole solutions that characterize black holes. The benefit is that the geometric horizons are intended be able to be extended to dynamical black hole solutions [6], and have already been shown to work on a number of exact solutions [19].

Cosmological Horizon

The cosmological horizon is the farthest distance in which a light ray can travel since the beginning of the universe (i.e. the big bang), this makes the cosmological horizon closely related to the apparent horizon. Since light has a finite upper limit on its velocity, objects that are too far apart cannot have interacted if the light travel time between them is less than the age of the current universe. Simply put, things beyond the cosmological horizon have not had enough time to interact with anything inside of it. This surface also defines the notion of the current 'observable universe'. Inside this surface, the expansion of outgoing null rays would be negative, relating this to the apparent horizon idea.

In general, not all of the solutions studied will contain astrophysical black holes, i.e. black holes for which the physics describing the equations is actually possible in the known universe. Though there is much mathematical interest in studying the dynamics of all systems resulting from the EFEs regardless of physicality.

1.1.7 Physical Simulations of Black Hole Interactions

A common method for determining the location of apparent horizons in simulations of black hole mergers and interactions is to use a null vector in the spacetime and locate the surface where the expansion of the null vector is zero. The main problem with this method is that the definition of a null vector in a spacetime intrinsically depends upon the foliation of the spacetime. This leads to a problem where the apparent horizon is not uniquely defined for a spacetime. We would like in general, to define a

surface that is characterized by invariants in the spacetime, and thus isn't dependent on the foliation. Utilizing the geometric horizon idea defined previously, using the Cartan-Karlhede algorithm to develop Cartan invariants for the spacetime allows us to define certain invariants related to the null expansion and use the vanishing of this particular curvature invariant to define the geometric horizon, and rather than the apparent horizon, use the geometric horizon for analysis. In the examples here, for a Quasispherical Szekeres spacetime, it turns out that the geometric and apparent horizons coincide, so the analogy here is rather useful for defining alternative methods for determining the special surfaces.

1.2 Newman-Penrose Formalism and the Frame Approach

Moving aside from the standard coordinate basis approach to writing down our equations for the metric and the curvature tensors and scalars, a method developed by Newman and Penrose [20] transforms the field equations into a larger set of first order differential equations by using an alternative to a coordinate basis to encode the curvature information.

1.2.1 The Null Frame

Moving into a frame formalism and away from coordinates like $\{t, x, y, z\}$, Newman and Penrose [20] opted to use a set of four null vectors, two real null vectors and two complex null vectors to replace the standard coordinate frame. The four frame vectors, called the tetrad, are typically denoted:

$$\{\ell, n, m, \bar{m}\} \tag{1.8}$$

where $\ell = \ell^\mu,\ n = n^\mu,\ m = m^\mu,\ \bar{m} = \bar{m}^\mu$ and where each of the frame vectors has the following properties:

$$\begin{aligned} \ell^\mu \ell_\mu = n^\mu n_\mu = m^\mu m_\mu = \bar{m}^\mu \bar{m}_\mu = 0 \\ -\ell^\mu n_\mu = 1 = m^\mu \bar{m}_\mu \end{aligned} \tag{1.9}$$

as well as all other inner products between the vectors being zero. The corresponding dual basis to the null tetrad is then easily seen to be

$$\Theta^i = \{-n, -\ell, \bar{m}, m\} \tag{1.10}$$

These tetrad vectors can be used to construct the null metric in the following way

$$g_{\mu\nu} = -2\ell_{(\mu}n_{\nu)} + 2m_{(\mu}\bar{m}_{\nu)} \tag{1.11}$$

where the brackets around the indices denote the symmetrization of those products:

$$\ell_{(\mu}n_{\nu)} = \frac{1}{2}\left(\ell_\mu n_\nu + \ell_\nu n_\mu\right) \tag{1.12}$$

In this frame, since the basis is the set of four null vectors, now the metric has components

$$g_{\mu\nu} = \begin{bmatrix} 0 & -1 & 0 & 0 \\ -1 & 0 & 0 & 0 \\ 0 & 0 & 0 & 1 \\ 0 & 0 & 1 & 0 \end{bmatrix} \tag{1.13}$$

The four directional derivative operators along the tetrad vectors are:

$$\begin{aligned} D &\equiv \nabla_\ell = \ell^a \nabla_a \\ \Delta &\equiv \nabla_n = n^a \nabla_a \\ \delta &\equiv \nabla_m = m^a \nabla_a \\ \bar{\delta} &\equiv \nabla_{\bar{m}} = \bar{m}^a \nabla_a \end{aligned} \tag{1.14}$$

The curvature information that is usually stored in the connection coefficients is now redefined as a set of twelve spin coefficients:

$$\begin{array}{lll} \kappa = -m^a D\ell_a & \pi = \bar{m}^a D n_a & \epsilon = -\frac{1}{2}\left(n^a D\ell_a - \bar{m}^a D m_a\right) \\ \sigma = -m^a \delta\ell_a & \nu = \bar{m}^a \Delta n_a & \gamma = -\frac{1}{2}\left(n^a D\ell_a - \bar{m}^a \Delta m_a\right) \\ \tau = -m^a \Delta\ell_a & \mu = \bar{m}^a \delta n_a & \beta = \frac{1}{2}\left(n^a \delta\ell_a - \bar{m}^a \delta m_a\right) \\ \rho = -m^a \bar{\delta}\ell_a & \lambda = \bar{m}^a \bar{\delta} n_a & \alpha = \frac{1}{2}\left(n^a \bar{\delta}\ell_a - \bar{m}^a \bar{\delta} m_a\right) \end{array} \tag{1.15}$$

1.2.2 Constructing a Null Frame from an Orthonormal Frame

From a standard coordinate frame, an inverse transformation (of the metric) to an orthonormal frame will give a set of orthogonal basis vectors which can be used then to construct the null frame in the following way

$$\begin{aligned} \ell &= \frac{e_0 + e_1}{\sqrt{2}} \\ n &= \frac{e_0 - e_1}{\sqrt{2}} \\ m &= \frac{e_2 - ie_3}{\sqrt{2}} \\ \bar{m} &= \frac{e_2 + ie_3}{\sqrt{2}} \end{aligned} \tag{1.16}$$

where $\{e_a\}$ are the basis elements of the orthonormal frame.

1.3 Curvature Tensors in the Null Frame

It is useful to talk about the Riemann curvature tensor, and its traceless part, the Weyl tensor in terms of their complex coefficients in the null frame. Where the Weyl tensor has the following components, given a null frame $\{l, n, m, \bar{m}\}$, defined by

$$\begin{aligned} \Psi_0 &= C_{abcd}\ell^a m^b \ell^c m^d \\ \Psi_1 &= C_{abcd}\ell^a n^b \ell^c m^d \\ \Psi_2 &= C_{abcd}\ell^a m^b \bar{m}^c n^d \\ \Psi_3 &= C_{abcd}\ell^a n^b \bar{m}^c n^d \\ \Psi_4 &= C_{abcd}n^a \bar{m}^b n^c \bar{m}^d \end{aligned} \tag{1.17}$$

The values of these 5 complex Weyl scalars encode the 10 independent components of the Weyl tensor and will determine the Petrov type of the spacetime, which will be used to put the null tetrad in a canonical form. For Petrov type D spacetimes, the Weyl scalars in a canonical frame take the form where

$$\begin{aligned} \Psi_0 = \Psi_1 = &\Psi_3 = \Psi_4 = 0 \\ &\Psi_2 \neq 0 \end{aligned} \tag{1.18}$$

Having the Weyl tensor in its canonical form will allow the construction of the preferred null frame for deriving Cartan invariants. And choosing a canonical frame

where we can determine the algebraic type of the spacetime allows us to further put conditions on these curvature invariants to locate the algebraically special geometric horizons. The Ricci tensor components are encoded into the set of complex scalars given by

$$\begin{aligned}
\Phi_{00} &= \frac{1}{2}R_{ab}\ell^a\ell^b,\ \Phi_{11} = \frac{1}{4}R_{ab}(\ell^a n^b + m^a\bar{m}^b) \\
\Phi_{22} &= \frac{1}{2}R_{ab}n^a n^b,\ \Phi_{01} = \overline{\Phi}_{10} = \frac{1}{2}R_{ab}\ell^a m^b \\
\Phi_{02} &= \overline{\Phi}_{20} = \frac{1}{2}R_{ab}m^a m^b \\
\Phi_{12} &= \overline{\Phi}_{21} = \frac{1}{2}R_{ab}m^a n^b \\
\Lambda &= \frac{R}{24}
\end{aligned} \tag{1.19}$$

where R is the Ricci scalar.

1.4 Lorentz Transformations

The set of Lorentz transformations that describe all transformations of the null frame includes null rotations about ℓ and n, spins about m and $\bar{m}$ and boosts on ℓ, n. The null rotations about ℓ (swapping $\ell \longleftrightarrow n$ gives the transformation for n):

$$\begin{aligned}
\ell' &= \ell \\
n' &= n + Em + +\bar{E}\bar{m} + |E|^2\ell \\
m' &= m + \bar{E}\ell \\
\bar{m}' &= \bar{m} + E\ell
\end{aligned} \tag{1.20}$$

where the rotation parameter E is complex, we can define a separate complex parameter B for null rotations about n. The spin and boost transformations, generalized as a spin-boost are

$$\begin{aligned}
\ell' &= \lambda\ell \\
n' &= \frac{n}{\lambda} \\
m' &= e^{i\theta}m \\
\bar{m}' &= e^{-i\theta}\bar{m}
\end{aligned} \tag{1.21}$$

The spin and boost parameters λ and θ are real. These transformations will be used to set the null frame in a canonical form. In total, the Lorentz group of transformations has 6 elements, two real parameters λ and θ, and four components of the E and B complex null rotation parameters. The number of elements of the Lorentz group that leaves a frame in its invariant form will be necessary for the procedure in the Cartan-Karlhede algorithm.

Chapter 2

Numerical Analysis

2.1 Root Finding

Various root finding methods were used according to the needs of each problem in this work. Overall a combination of two methods was often used. The main method for localizing roots to equations in one, two or three dimensions is the bracketing method. Where the easiest way to bracket the roots (not necessarily the most optimal, but was the most robust in all cases tested) was to check the product $F(x, C)F(x+h, C) < 0$, $C = const$ along sections of the surfaces in each dimension. This was the first step in all root finding problems over a subgrid spanning each dimension on the main grid for numerical analysis. It is noted that this method does not scale well with larger solution grids, though runtimes were not significant in the grand scheme (on the order of 1-5 minutes). The follow up method to refine the root locations depended upon the form of the equations given. The secant method was used for its robust nature and fast convergence, and to avoid situations where the derivatives of the functions became too high or too low for the Newton-Raphson method to be as effective as possible. The functions necessary for root finding in the examples all were functions of two variables.

2.2 Methods, Libraries and Software

The open source, peer reviewed C++ development libraries from Boost [21] were used mainly for the ordinary differential equation (ODE) integrator libraries, and the multiprecision library. Some of the research required numerical precision higher than the standard double floating point number, which only carries up to 16 decimal digits of precision. Typically calculations were done using 100 digits of precision for root finding on analytical solution surfaces due to the high number of significant figures required for the high degree polynomial function evaluated. Custom software

was written using the Boost C++ libraries for development of this work. Numerical integrations all used double precision variables. The computer algebra system Maple [18] was used for all tensor calculations, invariant calculations and transformations. A public repository of the code developed for this work is hosted on github [17].

2.3 ODE Integration

For the numerical problems considered, there were a set of integrators used to analyze the error properties of each solution. For all problems, the most robust numerical method used was the Dormand-Prince Runge-Kutta 4(5) step integrator with adaptive step size control and dense output.

The Dormand-Prince Runge-Kutta 4(5) (RKDP5) method was used for its error control properties, which give it a suitable stability for integrating all of the problems in this work [8]. The RKDP method is a Runge-Kutta family ODE solver in which the constants of all terms were chosen to minimize the error in the 5th order solutions. The 4th and 5th order solutions are then differenced to quantify the error of the method to the 4th order. This allows for convenient step-size control and grid resizing for all problems done here.

The overall method used for numerical analysis in this work employs use of the RKDP5 method, using adaptive step sizing to keep the error in control, then interpolating the solution points to a desired grid. The details of the internal workings of the interpolation method are given by the Boost organization [21], and are referred to as dense output steppers, as they can produce a continuous solution curve by numerical interpolation between solution points to any desired precision. The error order of this integrator is kept with absolute and relative tolerances at $\epsilon = 10^{-6}$.

Chapter 3

Quasi-spherical Szekeres Models

3.1 General Model

The general metric considered by Szekeres [25] is given by

$$ds^2 = dt^2 - e^{2\alpha}dz^2 - e^{2\beta}(dx^2 + dy^2) \tag{3.1}$$

where $\alpha = \alpha(t, z, x, y)$ and $\beta = \beta(t, z, x, y)$ are subject to the field equations. This metric describes a family of metrics that represent perfect fluid dust models, with zero pressure, and with cosmological constant Λ [25].

3.2 Quasi-spherical Szekeres Models

The quasi-spherical (QS) Szekeres models are forms of the Szekeres metric 3.1 where $\frac{\partial\beta}{\partial z} \neq 0$. With the parameterization given by Hellaby [14], and used in Bolejko [16, 24] the metric can be written in the form

$$ds^2 = -dt^2 + \frac{(R_{,z} - RH_{,z}/H)^2}{1 + 2E}dz^2 + \frac{R^2}{H^2}(dx^2 + dy^2) \tag{3.2}$$

the notation $()_{,z}$ denotes the partial derivative with respect to z, and where H is defined as

$$H \equiv \frac{S}{2}\left[\left(\frac{x - P}{S}\right)^2 + \left(\frac{y - Q}{S}\right)^2 + 1\right] \tag{3.3}$$

and $P(z), Q(z), S(z), E(z)$ are arbitrary functions and $R(t, z)$ is determined by solving the Einstein field equations. The function $H(z, x, y)$ is the term that breaks the spherical symmetry of the spacetime. The conditions where $S'(z) = Q'(z) = P'(z) = 0$ will bring the spacetime back to a spherically symmetric state.

3.2.1 Singularities in Szekeres Models

There are multiple types of singularities that can appear in Szekeres models, according to the description of the shells that make up the spacetime. Shell focussing singularities exist where $R(t,z) = 0$, and shell crossing singularities appear where $HR_{,z} - RH_{,z} = 0$. Both types of these singularities will be shown to be invariant features of the quasi-spherical Szekeres spacetime.

3.3 Lemaître - Tolman - Bondi Approximation

Reducing the Szekeres metric in (3.2), by applying the following definitions for S, P, Q

$$\begin{aligned} S(z) &= 1 \\ P(z) &= 0 \\ Q(z) &= 0 \end{aligned} \tag{3.4}$$

we get the Lemaître-Tolman-Bondi (LTB) metric

$$ds^2 = -dt^2 + \frac{R_{,z}^2}{1 - K(z)}dr^2 + R^2(dx^2 + dy^2) \tag{3.5}$$

Imposing the field equations with a dust source, this metric produces two field equations

$$\begin{aligned} 2M_{,z} &= 8\pi\rho R^2 R_{,z} \\ R_{,t}^2 &= \frac{2M}{R} - K + \frac{\Lambda R^2}{3} \end{aligned} \tag{3.6}$$

where $M = M(z)$, $K = K(z)$, $R = R(t,z)$, ρ is the energy density of the dust, and Λ is the cosmological constant. Thus we have an evolution equation for the dynamics of each shell, which are independent of each other, and another equation to determine the energy density.

3.4 Full Quasi-spherical Szkeres Field Equations

In analogy to the LTB solution, the Szekeres field equations can be written in the form [24]

$$\begin{aligned} 2\bar{M}_{,z} &= 8\pi\rho Y^2 Y_{,z} \\ Y_{,t}^2 &= \frac{2\bar{M}}{Y} - \bar{K} + \frac{\Lambda Y^2}{3} \end{aligned} \tag{3.7}$$

where $Y \equiv \frac{R}{H}$, $\bar{M} \equiv \frac{M}{H^3}$, $\bar{K} \equiv \frac{2K}{H^2}$. Also note that substituting the relation for Y back into the evolution equation gives us the exact same equation as in the LTB solution evolution equation for R (second part of equation (3.7)). An additional equation necessary for the analysis of shell crossings can be determined by taking the z derivative of the evolution equation (3.7)

$$\dot{R}_{,z} \equiv \dot{u} = \frac{1}{\dot{R}} \left(\frac{M_z}{R} - \frac{Mu}{R^2} + E_z + \frac{\Lambda R u}{3} \right) \tag{3.8}$$

where $u \equiv R_{,z}$, and the dot notation ($\dot{}$) denotes partial derivatives with respect to time. The solution to this equation gives $R_{,z}(t,z)$ and will be used for establishing shell crossing regions in the spacetime.

3.5 QS Szekeres Null Frame

Using the quasi-spherical metric for Szekeres, a null frame is developed for use in the Cartan-Karlhede algorithm. Starting with an orthonormal frame

$$\begin{aligned} e_0 &= -dt \\ e_1 &= W(t,z,x,y)dz \\ e_2 &= Y(t,z,x,y)dx \\ e_3 &= Y(t,z,x,y)dy \end{aligned} \tag{3.9}$$

where $W = \frac{(R_{,z} - RH_{,z}/H)}{\sqrt{1+2E(z)}}$, $Y = \frac{R(t,z)}{H(z,x,y)}$, the null frame has the form

$$\begin{aligned} \ell &= \frac{e_0 + e_1}{\sqrt{2}} = \frac{-dt + Wdz}{\sqrt{2}} \\ n &= \frac{e_0 - e_1}{\sqrt{2}} = \frac{-dt - Wdz}{\sqrt{2}} \\ m &= \frac{e_2 - ie_3}{\sqrt{2}} = \frac{Ydx - iYdy}{\sqrt{2}} \\ \bar{m} &= \frac{e_2 + ie_3}{\sqrt{2}} = \frac{Ydx + iYdy}{\sqrt{2}} \end{aligned} \tag{3.10}$$

and i is the imaginary component. The frame vectors m and $\bar{m}$ are complex null vectors, while ℓ and n are real null vectors.

3.6 Apparent Horizon Detection

A method of detecting the apparent horizon in the quasispherical Szekeres model by Debnath et al [7], was given in terms of a cubic function of the areal radius. The zeroes of this cubic function define the apparent and cosmological horizon, depending on the number of roots:

$$\Lambda R^3 + 3F(z) - 3R = 0 \tag{3.11}$$

where $F(z) = 2M(z)$ for this work. The number of and type of horizons that form in the spacetime are in terms of various conditions on F and Λ, also given by Debnath [7].

Table 3.1: Table of solutions to the horizon detector in equation (3.11), from Debnath et al.

Condition	Horizon Locations
1. $\Lambda = 0$	$R = 2M$
2. $F(z) = 0$	$R = 0, R = \pm\frac{1}{\sqrt{\Lambda}}$
3. $F(z) < \frac{2}{3\sqrt{\Lambda}}$	$R_1 = \frac{2}{\sqrt{\Lambda}}\cos(\theta/3)$ $R_2 = \frac{1}{\sqrt{\Lambda}}\left(-\cos(\theta/3) + \sqrt{3}\sin(\theta/3)\right)$ $\cos(\theta) = -\frac{3}{2}\sqrt{\Lambda}F(z)$
4. $F(z) = \frac{2}{3\sqrt{\Lambda}}$	$R = \frac{1}{\sqrt{\Lambda}}$
5. $F(z) > \frac{2}{3\sqrt{\Lambda}}$	No Horizon

For the examples in this work, specifying Λ gives situations where sections of the spacetime satisfy one or more of the conditions in Table (3.1). This results in multiple types of horizons forming. This behaviour will be examined further in Chapter 5.

Chapter 4

Cartan-Karlhede Algorithm

The method for constructing the set of Cartan invariants that characterize the spacetime involves defining a canonical frame for the system, then employing the Cartan-Karlhede algorithm [23]. This algorithm is used to determine the local equivalences of spacetimes, by comparing the Cartan invariants from each in a proper frame.

4.1 The Cartan-Karlhede algorithm

The algorithm involves computing the q^{th}-order derivative of the curvature tensor, and record the number of functional independent Cartan invariants at the q^{th} order, t_q. Then computing the dimension of the linear isotropy group, H_q. The linear isotropy group consists of the Lorentz transformations that leave up to the q^{th} order of the curvature tensor invariant.

The Cartan-Karlhede algorithm defined by MacCallum et al [23] , has the following procedure:

1. Start with the order of differentiation set to $q = 0$.
2. Calculate the derviatives of the Riemann tensor up to the q^{th} order.
3. Find the canonical form of the Riemann tensor and its covariant derivatives.
4. Fix the frame using the canonical form and noting the residual frame freedom, compute the dimension of H_q.
5. Find the number t_q of independent functions in the components of the Riemann tensor and covariant derivatives in the canonical frame.
6. If $dim(H_q) = t_q$, the algorithm stops. Else let $q = q + 1$ and continue from step 2.

4.2 Employing the Algorithm for the Szekeres Dust Spacetime

Zeroth Order

The zeroth order step of the algorithm starts with $q = 0$, and our null frame given by (3.10). Computing the Weyl tensor complex coefficients and the Ricci tensor components gives a set of independent functions. The isotropy group that leaves the weyl tensor invariant at zeroth order contains spins only, thus $dim(H_0) = 1$. In general there are two functionally independent Cartan invariants at this order. These are given by the scalars Φ_{00} and Ψ_2, the definitions of these terms are given in equations (1.17) and (1.19). The two scalars are functionally independent because they satisfy the following relation [5]

$$d\Phi_{00} \wedge d\Psi_2 \neq 0 \tag{4.1}$$

At the end of the zeroth order step, we have $dim(H_0) = 1$ and $t_0 = 2$.

First Order

At first order, we set $q = 1$ and continue the algorithm. The covariant derivative of the Weyl tensor contains the following algebraically independent quantities:

$$D\Psi_2,\ \Delta\Psi_2,\ \delta\Psi_2,\ \bar{\delta}\Psi_2,\ \rho,\ \mu,\ \kappa,\ \tau \tag{4.2}$$

The Ricci tensor also has the following independent scalars:

$$D\Phi_{22} + 4\epsilon\Phi_{22},\ \Delta\Phi_{22} - 4\epsilon\Phi_{22},\ \delta\Phi_{22},\ \bar{\delta}\Phi_{22} \tag{4.3}$$

The dimension of the isotropy group at first order is $dim(H_0) = 0$, because spins will effect the form of the spin coefficients ρ, κ, τ and anything that depends on the directional derivatives δ and $\bar{\delta}$. Choosing the frame where ϵ is real, using a spin, we are now in an invariant coframe, and the spin coefficients and frame derivatives of Ψ_2 and Φ_{22} can be worked with directly for establishing the set of Cartan invariants. From the sets of scalars above, we pick the largest set of independent functions, which is four, taking ϵ and $\bar{\pi}$ as our remaining functions and show that they are functionally

independent by the quadruple wedge product:

$$d\Phi_{22} \wedge d\Psi_2 \wedge d\epsilon \wedge d\bar{\pi} \neq 0 \tag{4.4}$$

The end of the second step of the algorithm concludes with $dim(H_1) = 0$ and $t_1 = 4$.

Second Order

At the second order, the second derivative of the weyl tensor admits the same size set of independent functions and dimension of the isotropy group as the previous step. Thus the algorithm concludes with $dim(H_2) = 0$ and $t_2 = 4$. The remaining Cartan invariants derived in this step are used as classifying functions that fully characterize the Szekeres dust models. For the purposes of the work here, these classifying functions are not necessary to detect geometric horizons. The appendix at the end of this work will contain an example of the computed set of invariants in terms of the metric functions in the QS Szkeres model.

4.3 Horizon Detection using Cartan Invariants

For the $\Lambda = 0$ case, the QS Szekeres models contain an apparent horizon, analogous to the Schwarzschild horizon, defined by the surface $R = 2M$. For $\Lambda \neq 0$, this can be generalized to the cubic function in equation (3.11). From the set of Cartan invariants, the spin coefficients ρ and μ will be used as generalized apparent horizon detectors. These spin coefficients will be shown to have the same zero sets as $R = 2M$ and (3.11).

Using the Bianchi identities to simplify, the non zero components of the covariant derivative of the Weyl tensor are given in terms of the scalars:

$$\begin{aligned} C_{1214;3} = C_{1434;3} = C_{1213;4} = C_{1334;4} &= 3\rho\Psi_2 \\ 2C_{1423;1} = C_{1212;1} &= C_{3434;1} \\ C_{3434;1} = = &\frac{-2\Delta\Phi_{11} - 32\epsilon\Phi_{11} - 4\mu\Phi_{11} + \rho(18\Psi_2 + 4\Phi_{11})}{3} \end{aligned} \tag{4.5}$$

The terms ρ and μ are related to the ingoing and outgoing null expansions, and

the surface where $\rho \leq 0$ and $\mu = 0$ (for the collapsing phase vice-versa for the expanding phase) define the geometric horizon. In terms of comparing the geometric and apparent horizons, in this case they coincide, but in general the surfaces are distinct. [5] From the terms in the covariant derivative of the Weyl tensor, we see that having $\rho = 0$ ($\mu = 0$ in collapsing phase) makes the Weyl tensor more algebraically special, and this means we can use ρ (μ) to locate the geometric horizon. The condition for the geometric horizon changing from $\rho = 0$ to $\mu = 0$ for the collapsing phase can be seen by comparing the functional forms (see Appendix equations 6.11, 6.12) of these spin coefficients, and noting that the change from the expanding to collapsing phases results in a sign change of $R_{,t}$, meaning that only one of these spin coefficients will have a zero set at a time in this spacetime.

Properties of the Spacetime in terms of Cartan Invariants

Since any function constructed by the set of Cartan invariants is also a Cartan invariant, there are a set of properties of the metric that can be realized as invariants. Taking the Ricci and Weyl scalars from the zeroth order step of the algorithm, we can define

$$C_0 = \Psi_2 - \frac{\kappa\bar{\rho}}{12} = \frac{-M}{2R^3} \tag{4.6}$$

Now using the spin coefficients ρ and μ, and defining two more Cartan invariants

$$C_1 = -\sqrt{2}\frac{(\rho + \mu)}{2} = \frac{\sqrt{1 + 2E}}{R} \tag{4.7}$$

$$C_2 = -\sqrt{2}\frac{(\rho - \mu)}{2} = \frac{R_t}{R} \tag{4.8}$$

Using the evolution equation (3.7), we combine the Cartan invariants

$$-4C_0 + C_1^2 - C_2^2 = \frac{1}{R^2} \tag{4.9}$$

Showing that the areal radius is an invariantly defined function.

The mass and energy functions M and E are also Cartan invariants since they can be defined in terms of Cartan invariants in the following way:

$$M = -2C_0R^3 \tag{4.10}$$

$$E = \frac{C_1^2R^2 - 1}{2} \tag{4.11}$$

In addition, the quantity C_2 (4.8) defines the expansion and contraction of spacetime, analogous to the Hubble parameter.

4.4 Shell Crossing Detectors as Cartan Invariants

Shell crossing singularities appear in these models where the metric function

$$\sqrt{g_{zz}} = \frac{R_{,z} - \frac{RH_{,z}}{H}}{\sqrt{1+2E}} \tag{4.12}$$

has a vanishing numerator. This condition also corresponds to the divergence of the density, since from the field equations (3.7),

$$\tilde{\rho} = \frac{M_{,z}}{4\pi Y^2 Y_{,z}} \tag{4.13}$$

So to find a suitable detector for the shell crossings, it seems useful to consider the inverse of the density:

$$C_3 = \frac{1}{\tilde{\rho}} = \frac{4\pi Y^2 Y_{,z}}{M_{,z}} \tag{4.14}$$

This function is defined in terms of Cartan invariants, and also vanishes when shell crossings occur. In general this property will be used for detecting shell crossing singularities in the spherical and quasi-spherical cases.

Chapter 5

Numerical and Analytic Models of Black Hole Formation

5.1 Field Equations for a Dust Model

The Quasi-spherical Szekeres field equations are given by (3.7)

$$\begin{aligned} 2\bar{M}_z &= 8\pi\tilde{\rho}Y^2Y_z \\ \dot{R}^2 &= \frac{2M}{R} - K + \frac{\Lambda R^2}{3} \end{aligned} \tag{5.1}$$

where the functions $M(z)$ and $K(z)$ are arbitrary functions to be defined for each example, and the dot notation refers to the time derivative, and $Y \equiv \frac{R(t,z,x,y)}{H(z,x,y)}$. $\tilde{\rho}(t,z,x,y)$ is the energy density of our dust source, and $R(t,z)$ is the areal radius of each shell of matter in the spacetime. The positive root of the $\dot{R}$ equation describes the expanding phase of the solution, and the negative root describes the collapsing phase. In the remaining work, the coordinate r has been relabelled to z.

5.2 Primordial Black Hole Formation

Here we are extending a model by Harada and Jhingan [11] for primordial black hole (PBH) formation, and introducing a non-zero cosmological constant, and utilizing the Cartan invariants derived for the Szekeres spacetime, and including the apparent horizon detector from Debnath to analyze formation of the geometric horizons, and how they compare to the apparent horizons.

Choosing M(z) and K(z)

The arbitrary functions $M(z)$ and $K(z)$ are chosen to correspond to the choices by [11, 16], where $K(z) \equiv -2E(z)$ and $M(z)$ given by model D in the work of [11], which was developed mainly for having shell crossings appearing interior to the apparent horizons for primordial black holes in Szekeres spacetimes with zero cosmological

constant.

$$\begin{aligned} M(z) &= \frac{z^3}{2} \\ E(z) &= \frac{1}{2}\left(\frac{z}{r_c}\right)^2 \left(1 + \left(\frac{z}{r_w}\right)^{n_1} - 2\left(\frac{z}{r_w}\right)^{n_2}\right)^4 \end{aligned} \tag{5.2}$$

with $n_1 = 8$, $n_2 = 10$, $r_c = 10$, $r_w = 1$, and z restricted to the domain $z \in (0, 1)$. $E(z)$ has been chosen such that $E(z) < 0 \ \forall z \in (0, 1)$. The choices of M(z) and E(z) above will not qualitatively change the dynamics of the shells on their own, but will affect where and when shell crossings appear in the system. Modifying the n_1 and n_2 parameters in (5.2) changes the time at which shell crossings start to occur in the spacetime. The effect of these parameters changing is shown in figure (5.12).

Deviation from Spherical Symmetry

The quasispherical condition for this problem was chosen by setting $S(z) = \sqrt{2}z$, keeping $P = Q = 0$. The shells of matter with these conditions are still concentric, but no longer spherically symmetric, as $S' \neq 0$ [4]. Setting the function $S(z) = 1$ recovers an LTB seed solution [5], with full spherical symmetry. This spherically symmetric condition will be used for some of the shell crossing images for viewing in two dimensions.

5.2.1 Exact Solution

For the field equations in (5.1), with $\Lambda = 0$ we have an exact solution for $R(t, z)$ that is parameterized by $\eta(t, z)$ for the case with $E(z) < 0$, whose solution is written explicitly by [24, 16], in the elliptic case

$$\begin{aligned} R &= -\frac{M(z)}{2E(z)}\left(1 - cos(\eta)\right) \\ \eta - sin(\eta) &= \frac{(-2E)^{3/2}}{M}(t - t_B(z)) \end{aligned} \tag{5.3}$$

where $\eta(t, z) \in [0, 2\pi]$ parameterizes time, and $t_B(z)$ is an arbitrary function that defines the time locus of the big bang for each point in space. For this problem $t_B(z) = 0$, to model primordial black hole formation just after the time of the big bang.

The proper time parameterization functions for each phase of the solution are given by [24, 15, 16]

$$t = t_B(z) + \frac{M}{(-2E)^{3/2}} \left(cos^{-1}(u) - sin(cos^{-1}(u)) \right) \tag{5.4}$$

where u is defined by

$$u \equiv 1 + \frac{2ER}{M} \tag{5.5}$$

This simplifies for the expanding phase to

$$t = t_B(z) + \frac{M}{(-2E)^{3/2}} \left(cos^{-1}(u) - \sqrt{1-u^2} \right), \quad \eta \in [0, \pi] \tag{5.6}$$

And similarly for the collapsing phase

$$t = t_B(z) + \frac{M}{(-2E)^{3/2}} \left(\pi + cos^{-1}(-u) + \sqrt{1-u^2} \right), \quad \eta \in [\pi, 2\pi] \tag{5.7}$$

Initial Conditions

From the expressions in equations (5.6) and (5.7), setting $t = t_B = 0$ gives an expression to solve for R when $t = 0$. This was done numerically using the tools and methods described in Chapter 2.

Shell Crossing Formation

For shell crossings to occur in this model, we require the term $R_z - RH_z/H$ to vanish, this also corresponds to a state where the density of the matter is divergent. Because of the spherical symmetry for each individual shell, when neighbouring shells cross, one would expect some circular type of surface to form. Taking the equation for the shell crossings, noting that there is a Cartan invariant (C_0) that detects this behaviour, we can derive the conditions on the equations to form a shell crossing, given the dipole terms S, P, Q.

$$R_z - \frac{RH_z}{H} = 0 \tag{5.8}$$

Given the full form of the H term, generalized with the dipole terms $P = Q = 0$, and using a prime in place of the z derivative subscript, this equation can be written

$$HR' - RH' = \frac{R'S}{2}\left[1 - \frac{x^2+y^2}{S^2}\right] - \frac{RS'}{2}\left[1 + \frac{x^2+y^2}{S^2}\right] = 0 \tag{5.9}$$

and solving for $(x^2 + y^2)$ results in the equation for a circle in the projective plane, for a given z

$$x^2 + y^2 = \frac{S^2(S'R - SR')}{SR' + S'R} \tag{5.10}$$

This shows that the shell crossings in the projective plane appear as circles, with radius

$$R_{SC} = \sqrt{\frac{S^2(S'R - SR')}{SR' + S'R}} \tag{5.11}$$

with the condition that $S > 0$, this gives a condition to check to see if at any point in the time solutions, shell crossings appear, and when they do, what radius they have in the projective plane.

$$S'R - SR' > 0 \tag{5.12}$$

equation (5.12) is the condition where shell crossings will appear in the system. For a particular choice of dipole term, we can see that this relation can also be rewritten as

$$\frac{R'}{R} < \frac{S'}{S} \tag{5.13}$$

Introducing the other dipole terms P, Q will of course change the behaviour of the shell crossings here, by shifting the center of the shell in the projective plane to $(-P, -Q)$. The behaviour on the form of the shell crossings is still circular, though the center of the shell crossing center depends on the values of P, Q, P', Q'. For a set of initial conditions, this condition on the shell crossing formation was used to check where shell crossings appear in the domain. If we turn back to spherical symmetry, $S' = P' = Q' = 0$, we can see that the condition for shell crossings happens to be $R_{,z} \leq 0$, as expected when comparing to an LTB seed solution. Both conditions will

be used for checking the formation of shell crossings in the LTB seed and the full quasispherical problem.

Apparent and Cosmological Horizon Formation

Following the analysis done with the Cartan-Karlhede algorithm, the geometric horizons are detected on the algebraically special surface defined by $\mu = 0$ in the collapsing phase, the apparent horizons are detected by the cubic function for R given by Debnath [7]. The cosmological horizon in these cases is a special case solution satisfying specific conditions given by Table 3.1. The zero sets for these horizons were calculated numerically following the methods described in Chapter 2.

5.2.2 Numerical Solutions

Initial Conditions

From the exact solution for $R(t, z)$ in the $\Lambda = 0$ case, it can be seen that the maximum shell radius for each point in space occurs at the parameter value $\eta = \pi$, which corresponds to the start of the collapsing phase of the problem. This condition results in the maximum areal radius given by

$$R_{max} = -\frac{M(z)}{E(z)} \tag{5.14}$$

This particular choice of $R(z)$ also happens to be a critical point for the $\Lambda = 0$ problem, so numerical analysis done on that problem for comparison cannot utilize the same initial conditions. This point for R is not a critical point in the $\Lambda \neq 0$ case due to the introduction of the $\frac{\Lambda R^2}{3}$ term. This initial condition was a choice in the numerical work to be somewhat relevant as compared to the exact solution, and other initial conditions will be employed further on in the analysis.

For the $R_z(t)$ evolution equation (3.8), the initial conditions were simply the z derivative of the $R(0, z)$ condition above.

$$R_z(0, z) = u(0, z) = -\frac{M_z(z)}{E(z)} + \frac{M(z)E_z(z)}{E(z)^2} \tag{5.15}$$

where the functional forms of $E(z)$ and $M(z)$ are given in equation (5.2).

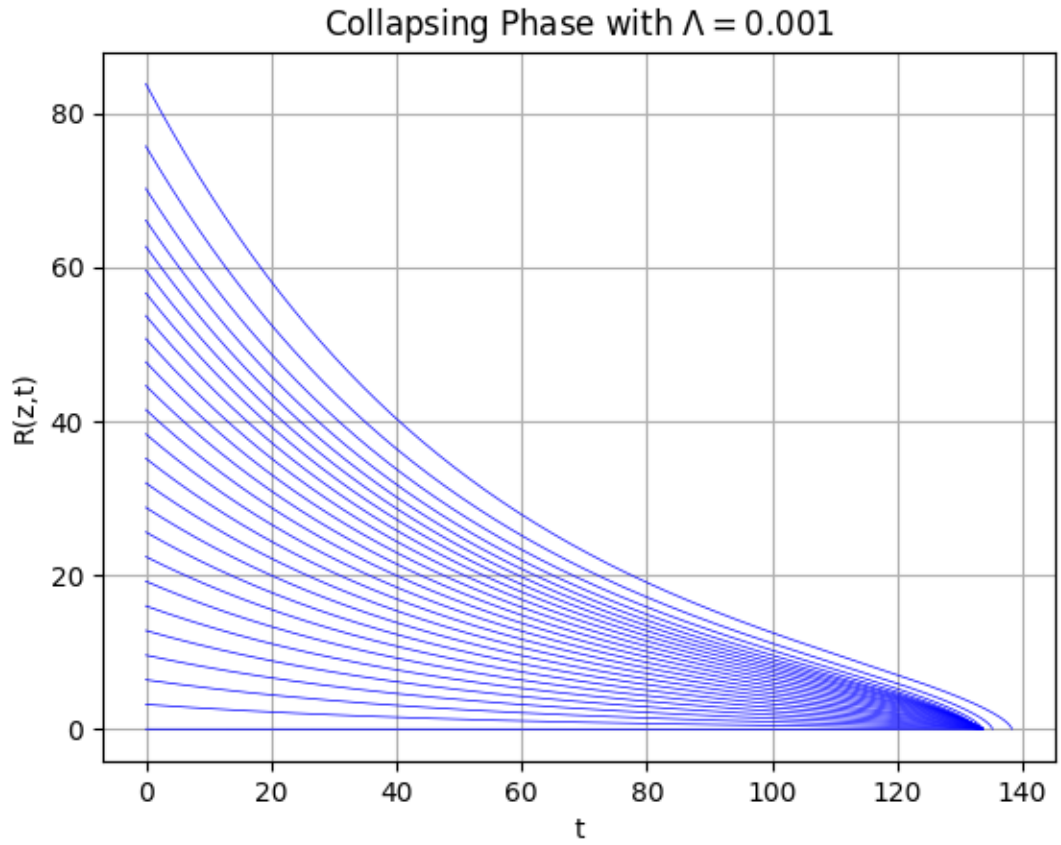

Figure 5.1: Shell evolution of the PBH Model. Shells corresponding to initial conditions in equation 5.14.

Shell Evolution and Horizon Formation

Since all horizon detectors (ρ, μ, and the apparent horizon detector by Debnath [7]) only depend on the areal radius $R(t, z)$, the formation and growth of the horizons can be shown simply in two dimensions. The figures (5.1, 5.2, 5.3, 5.4) show the contraction of the shells towards the shell focussing singularity, from their initial conditions, for various values of Λ.

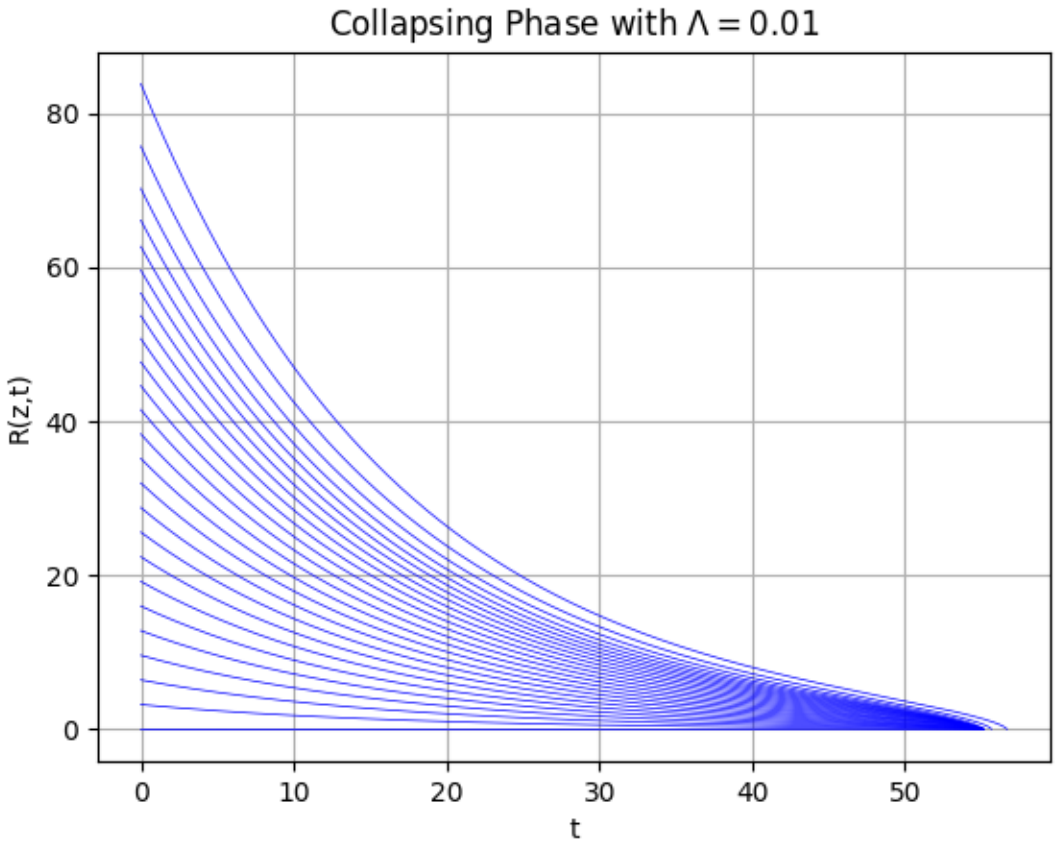

Figure 5.2: Shell evolution of the PBH Model. Shells corresponding to initial conditions in equation 5.14.

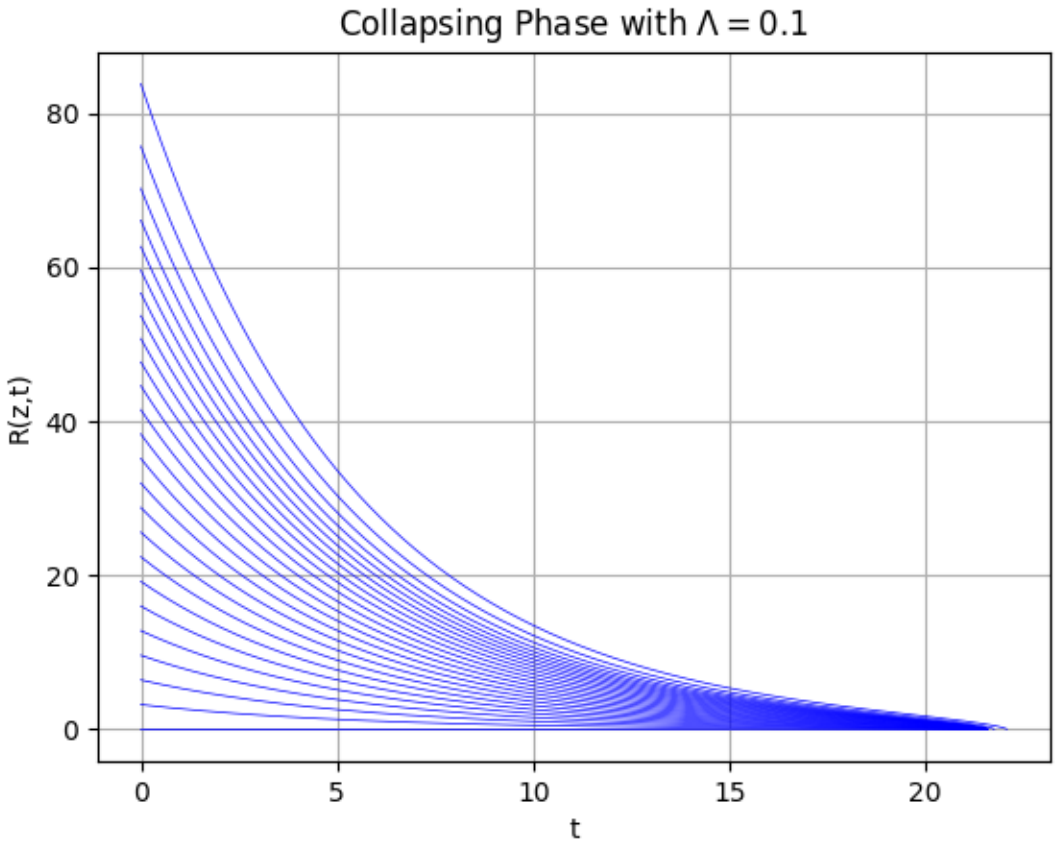

Figure 5.3: Shell evolution of the PBH Model. Shells corresponding to initial conditions in equation 5.14.

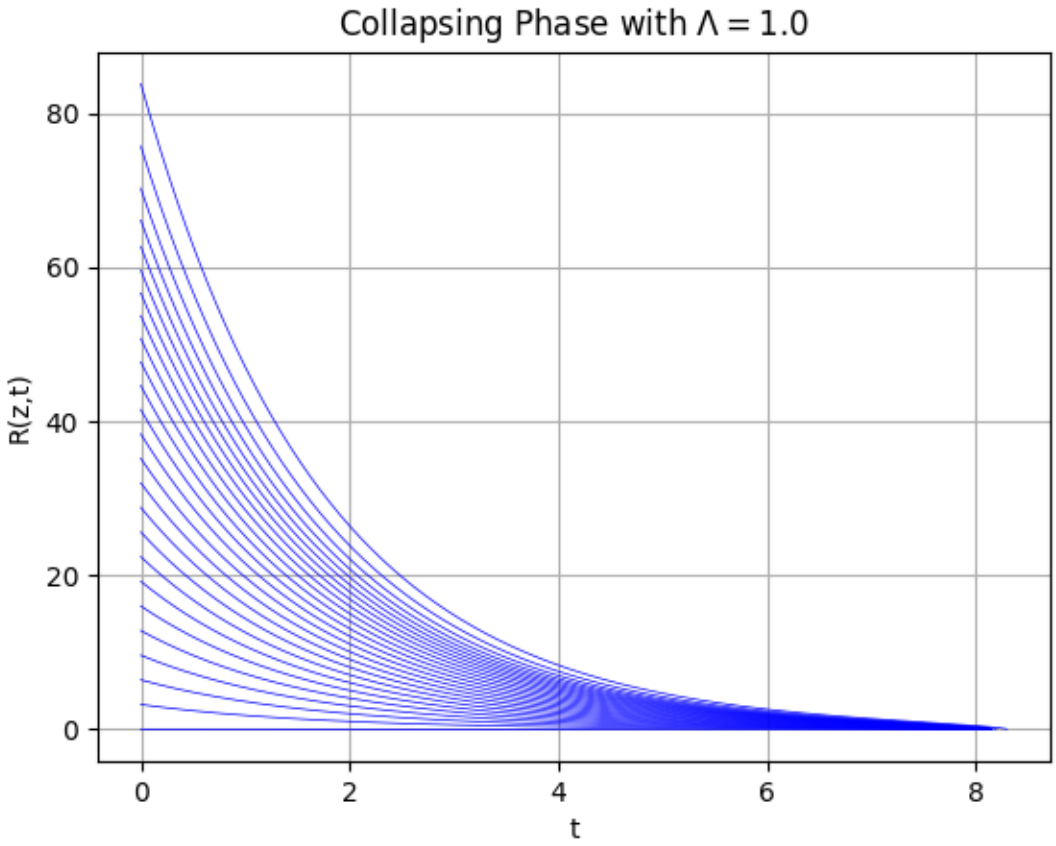

Figure 5.4: Shell evolution of the PBH Model. Shells corresponding to initial conditions in equation 5.14.

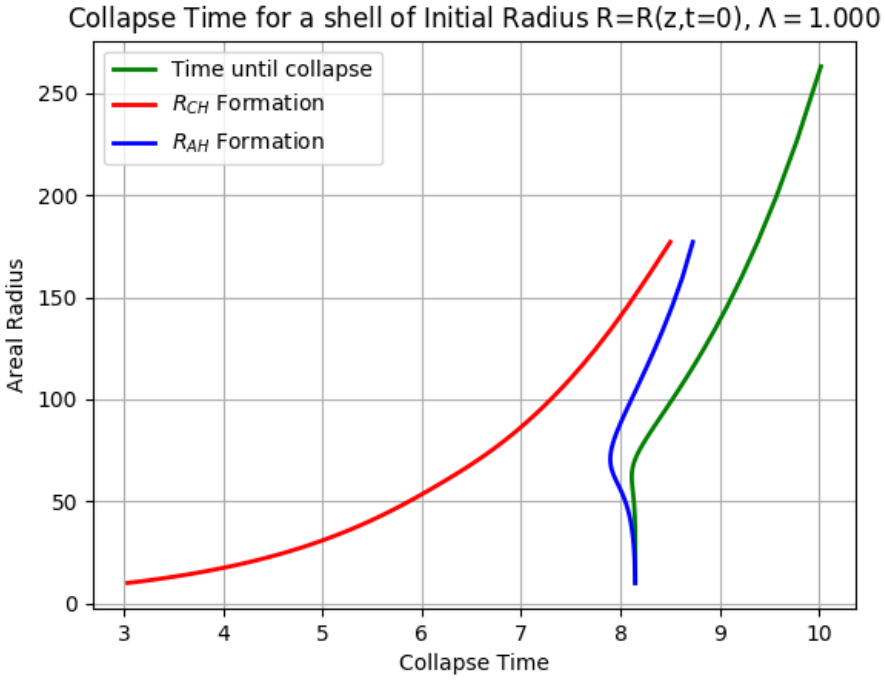

Figure 5.5: Collapse time for a shell with initial radius $R(t = 0, z)$. Also shown are the time until formation of the cosmological and apparent horizons from each initial condition.

Collapse Time and Surface Formation Time

Plotting the time for a shell with initial areal radius $R(t = 0, z)$ to collapse is shown in figures (5.5) and (5.6). The time until each shell has passed through the cosmological and apparent horizons is also shown. Because of the horizons merging and disappearing after a finite time, not every shell in the spacetime will pass through a horizon before merging into the shell focus at $R = 0$.

Comparing Curvature Invariants with the Apparent Horizon Detector by Debnath

The apparent horizon detector given by Debnath [7] in equation (3.11), with exact solutions in Table (3.1) and numerical solutions, compared with the zero set of the Cartan invariant μ gives a way to compare the effectiveness of the Cartan invariants in detecting horizons. And also shows that the apparent horizon is also a geometric horizon [6, 5].

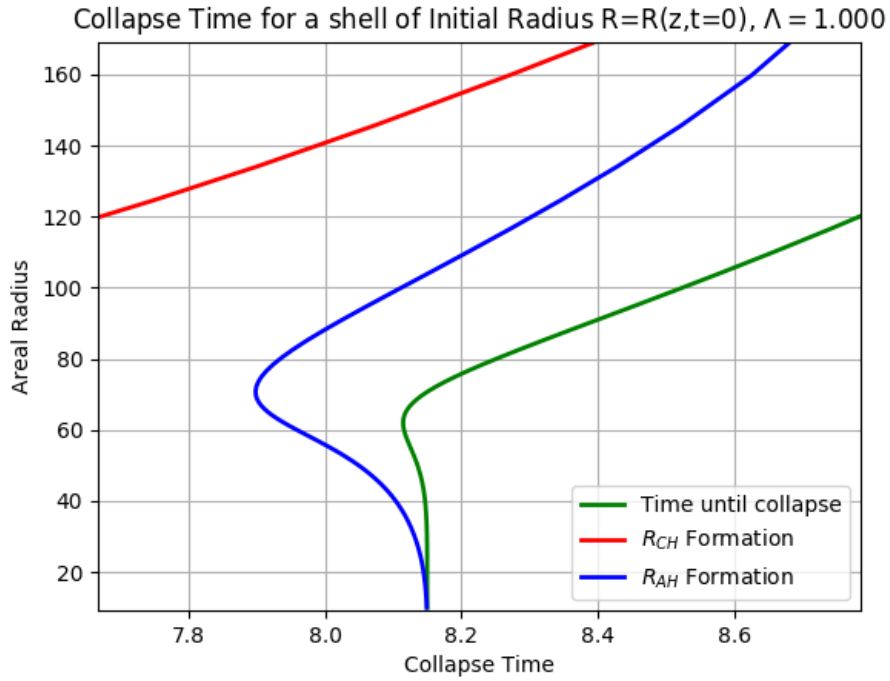

Figure 5.6: Collapse time for a shell with initial radius $R(t = 0, z)$. Also shown are the time until formation of the cosmological and apparent horizons from each initial condition. Zoomed in near the formation of the shell focussing singularity, the apparent horizon forms shortly before the shells have collapsed fully from the inner region of the initial spacetime.

For cases where there is a cosmological horizon and an apparent horizon in the solution, the zero sets of μ and equation (3.11) reflect the formation of this extra surface. Setting $\Lambda = 1$, with the initial condition given by equation (5.14)

Some values of Λ admit up to three separate horizons that exist for finite periods of time in these solutions, here is an example with $\Lambda = 1.695$, initial conditions as in (5.14). For situations where there is a second (or sometimes third) MOTS forming at a particular time, the smallest MOTS that collapses down to the singularity is distinct from the apparent horizon and cosmological horizon, and in general is a temporary MOTS that always disappears in a finite time after the apparent horizon forms.

Shell Crossing Formation and Initial Conditions

In the LTB seed solution, which is the reduction from QS Szekeres to LTB by letting $S = 1,\ P = 0,\ Q = 0$, the condition for shell crossings simplifies to

$$R_{,z} = 0 \tag{5.16}$$

Using this condition, we can visualize shell crossings in the LTB solution, as a reference for the QS Szekeres model, before moving on to the full inhomogeneous model.

For the initial conditions chosen in equation (5.14), the shells initially are crossing if we apply a dipole term $S(z) = \sqrt{2}z$ to deviate from spherical symmetry. This can be easily seen by checking the inequality (5.13). The inequality is shown in Figure (5.11).

A modification to the $E(z)$ function given by Jhingan and Harada [11] model D will put the models in a better initial position with no immediate shell crossings. Modifying the n_2 parameter provides another set of initial conditions where there is at least no shell crossing initially. These updated initial conditions are shown in Figure (5.12).

Moving up to the full QS Szkeres solution, visualizing the shell crossings becomes much more of a difficult task, the following figures show the shell crossings in the solution for a single shell, in the projective plane (x, y), defined by the shell crossing condition in equation (5.13). Using the condition (5.8), plotting for a shell at location z, with areal Radius $R(t, z)$ at time t, the shell crossings can be seen where there are roots of this function.

5.3 Galactic Black Hole Formation

An extension of the galactic black hole model by [16], introducing a non-zero cosmological constant. The model is a generalization of LTB like models, and here is used to describe the formation of a galactic black hole. Parameters and functions are chosen so that no shell crossings appear in any of the models, at least for the $\Lambda = 0$ case, and will be shown to also not contain shell crossings if this constraint on Λ is lifted. Choosing coordinates where $\bar{z} = M(z)$, we essentially let the z coordinate be the mass of the shell. Setting $z = M$, and defining the bang and crunch time arbitrary functions from the exact solution:

$$t_B(M) = -bM^2 + t_{B_0}, \quad t_C(M) \quad = aM^3 + T_0 + t_{B_0} \tag{5.17}$$

where t_B and t_C are the bang and crunch time functions respectively, a, b, t_{B_0}, T_0 are arbitrary constants. T_0 is the measure of time between the big bang and the big crunch along the line $M = 0$, and t_{B_0} is the time coordinate for the central point of the big bang. Using these functions, the function $E(M)$ can be written simply as:

$$2E(M) = -\frac{(8\pi M)^{2/3}}{4^{2/3}(aM^3 + bM^2 + T_0)^{2/3}} \tag{5.18}$$

Initial Conditions

The initial conditions determined for this problem utilize the exact solution 5.3, plugging in the functions defined above, and solving for R when $t = 0$ numerically, using a bracketing-secant method. The exact solutions for this problem were difficult to solve for initial conditions numerically on standard double precision, due to the sharp asymptotic behaviour of the function near $t = 0$. Using higher precision floating point type numbers helped overcome the issue with root finding on the exact solution, and it was determined that 100 decimal digits of floating point precision were enough to properly work the root finding methods.

The results shown in figure 5.14 show that the apparent horizon and geometric horizon also coincide in this example. As established before, it turns out that the apparent horizon in this model is also a geometric horizon. This feature is not generalized to other models, because of the difference in the way the horizons are defined,

they aren't necessarily going to coincide.

Adding a non-zero cosmological constant to this system yields some interesting results. Similar to the primordial black hole example, certain ranges of values for the cosmological constant will result in no horizons forming in certain regions of the spacetime, and horizons that will disappear after a finite time.

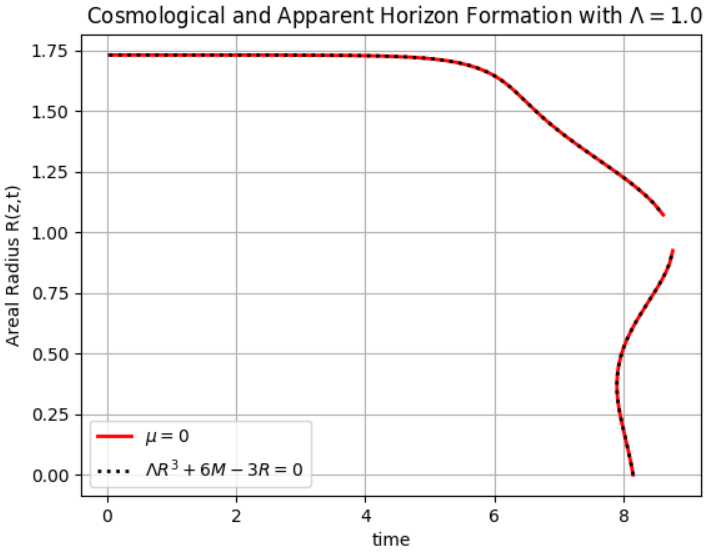

(a)

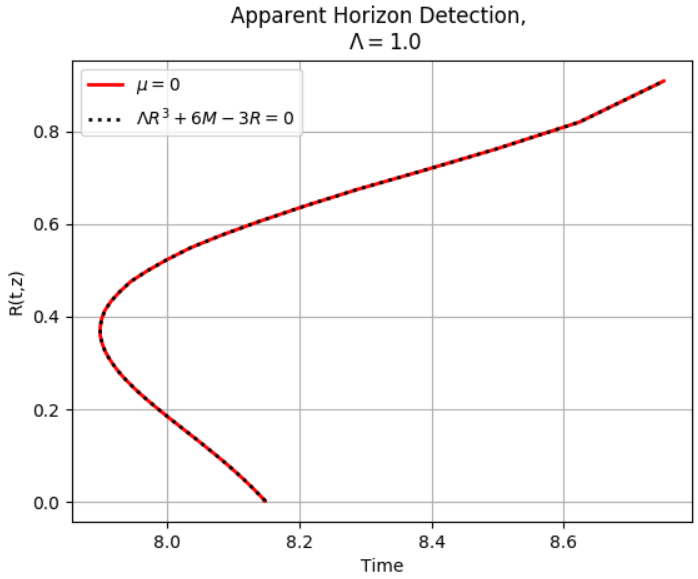

(b)

Figure 5.7: PBH example. Cosmological and Apparent horizon formation, satisfying in with case 3 in Table 3.1. The horizons in this case start to merge after the formation of the apparent horizon. In Table 3.1, the spacetime is covering different cases where different numbers of horizons appear. The value of Λ satisfies the condition that the horizons merge at a location inside the domain $z \in (0, 1)$. Numerical resolution from choices of initial conditions were particularly hard to choose to find the right shell that is on the horizon near the merger times. on the lower figure, zoomed in to the apparent horizon, the upper branch of the curve is the apparent horizon, and the lower branch that falls into the singularity is another MOTS in the spacetime.

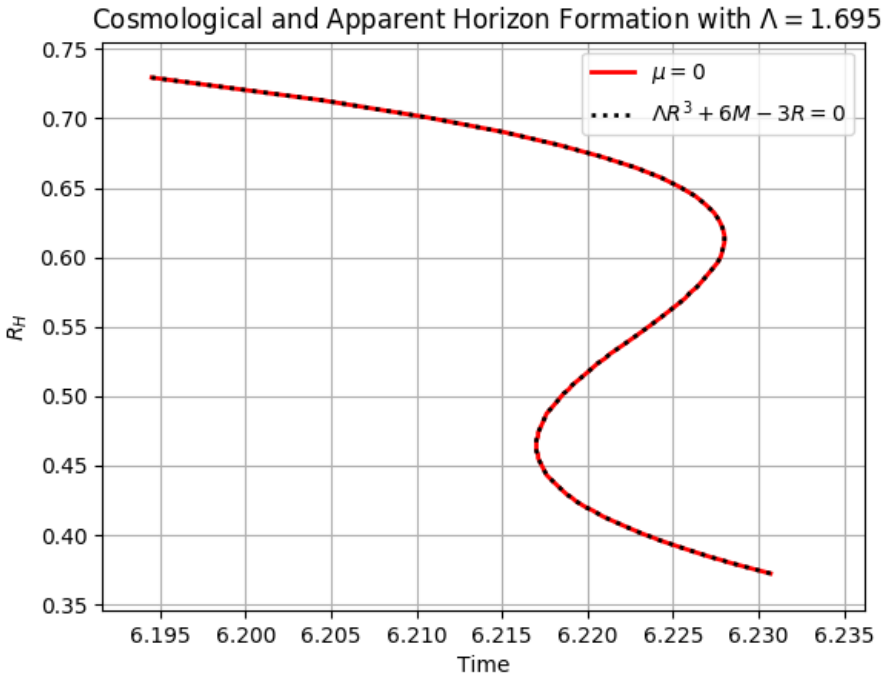

Figure 5.8: PBH formation. $\Lambda = 1.695$ model zoomed in to a region showing three horizon surfaces for a finite time. These surfaces collapse down to the shell focus. During times where there are three MOTS in the spacetime, the largest MOTS is the cosmological horizon, the middle MOTS is the apparent horizon, and the inner surface is just an interior MOTS that collapses to the singularity.

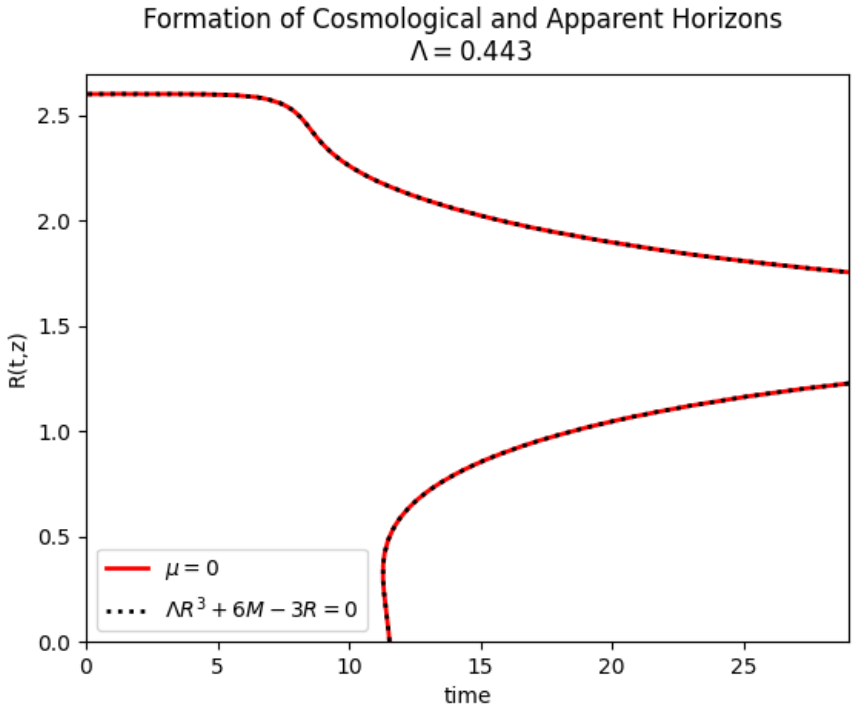

Figure 5.9: PBH formation. The solution space satisfies the case where there are always two horizons. The larger (top red/black line) one corresponds to the cosmological horizon, and the smaller (bottom red/black line) is the apparent horizon surround the shell focussing singularity. For a short time after the apparent horizon forms, there is a third MOTS that collapses down quickly into the singularity. $\Lambda = 0.443$ chosen so that the horizons would merge just beyond the domain. The horizons asymptote together over time.

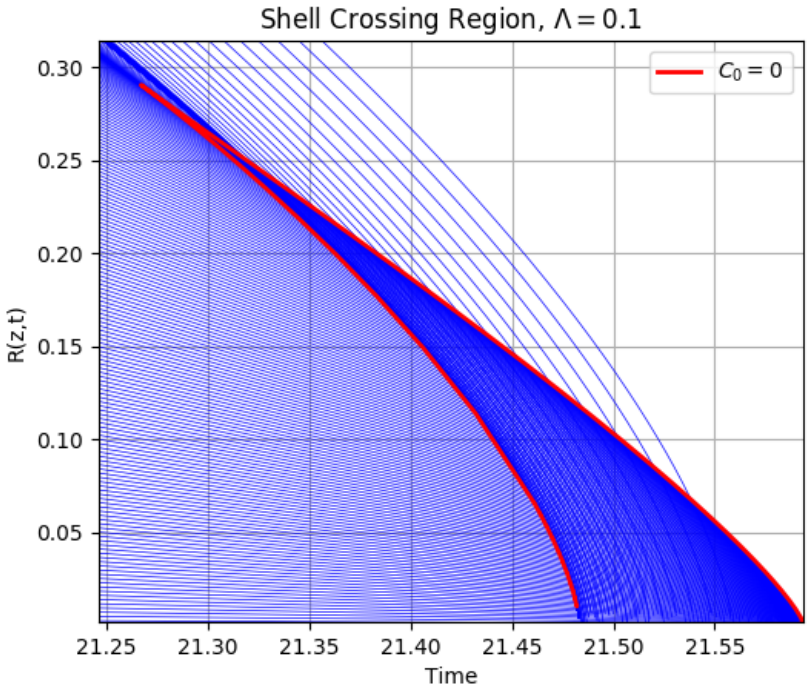

Figure 5.10: PBH formation. Shell crossing region when reduced to the LTB solution, plotting the zero set of the shell crossing detector. In this image, 200 shells were evolved to achieve the resolution necessary on the zero set of the shell crossing detector. Clearly it shows that the shell crossing detector surrounds the entire shell crossing region.

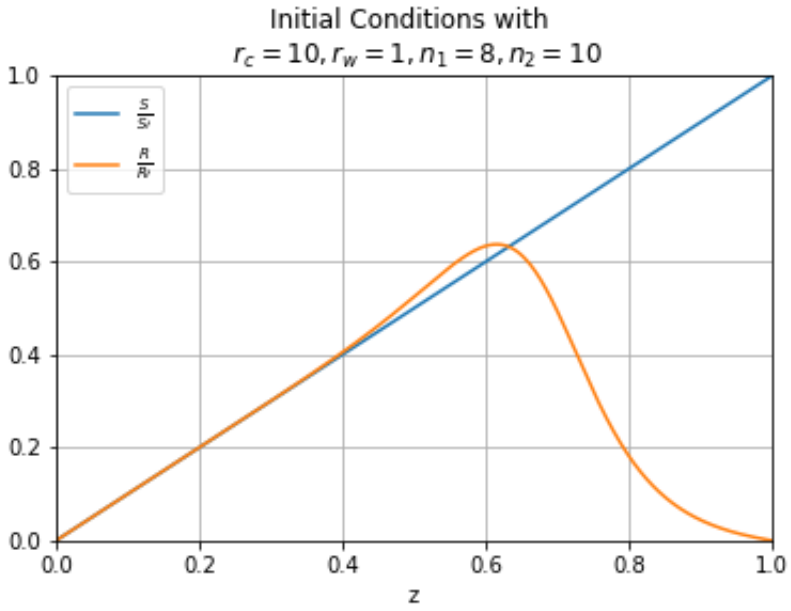

Figure 5.11: PBH formation. Initial conditions in (5.14). Parts of the curve above the $y = z$ line are shells which currently have shell crossings, following the condition in (5.13).

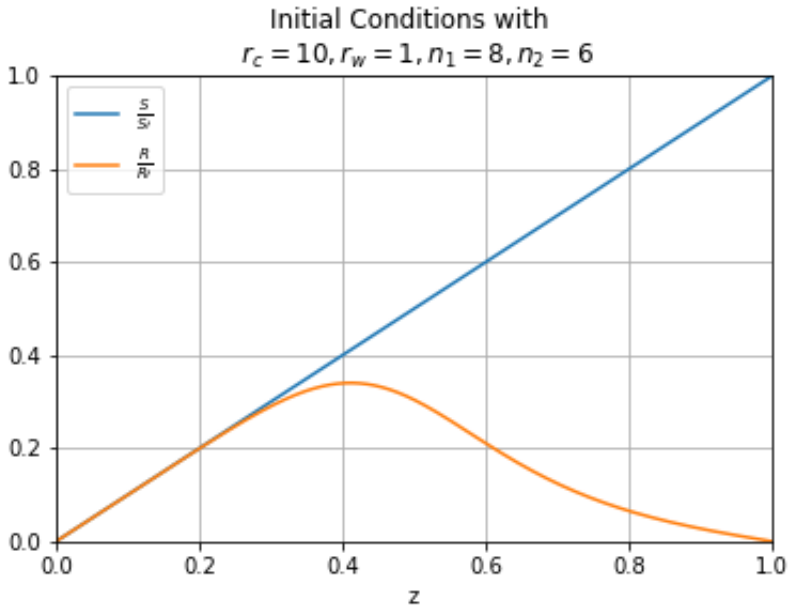

Figure 5.12: PBH example with modified energy function $E(z)$, for the quasispherical case with $r_c = 10$, $r_w = 1$, $n_1 = 8$, $n_2 = 6$. Parameters chosen so that at least initially, there are no shell crossings in the model. There is a lot of control left to choosing a shell distribution so that shell crossings won't occur for some time

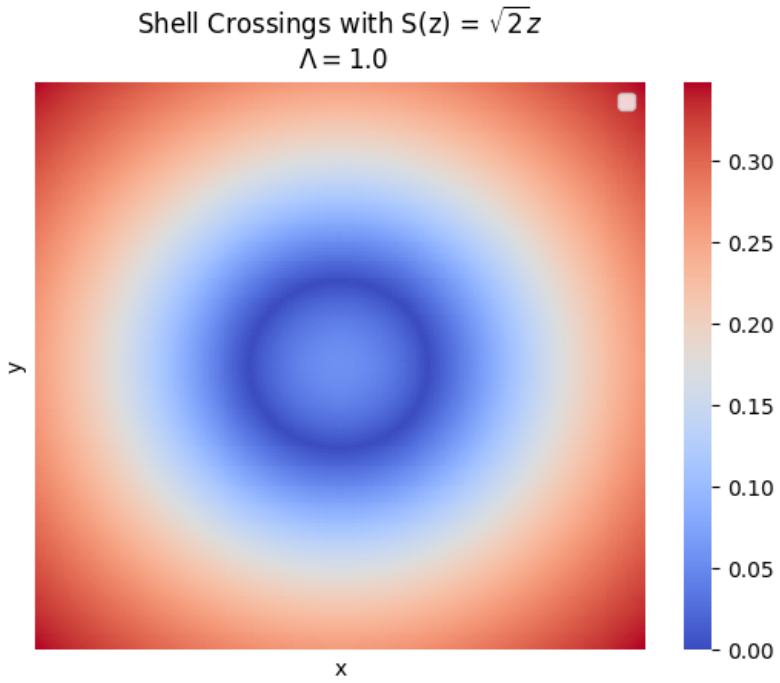

Figure 5.13: PBH formation example. A plot of $|Y_{,z}|$ in the projective plane. The shell crossing appears as a circle in the projective plane;. The colour bar corresponds to the height of the function $|Y_{,z}|$. Roots of this function are locations where the density is infinite. The shell crossing appears as a ring (in dark blue), and has a radius corresponding to the shell crossing radius condition in (5.13). The central region interior to the shell crossings has $Y_{,z} < 0$.

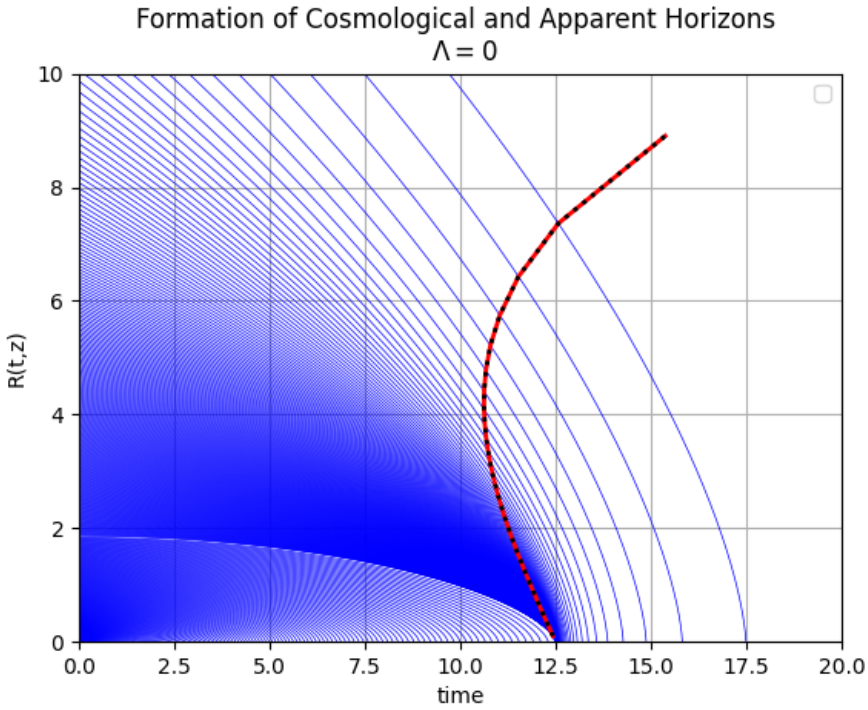

Figure 5.14: Galactic black hole formation. Apparent and geometric horizon formation indicated by the zero set of the Cartan invariant μ (solid red line), and additionally, the surface $R = 2M$ (black dashed line) which is the location of the MOTS in this model. No shell crossings appear for $\Lambda = 0$. The apparent horizon is the upper branch of the dashed line that is increasing in size over time, and the inner branch is a secondary MOTS that collapses into the singularity.

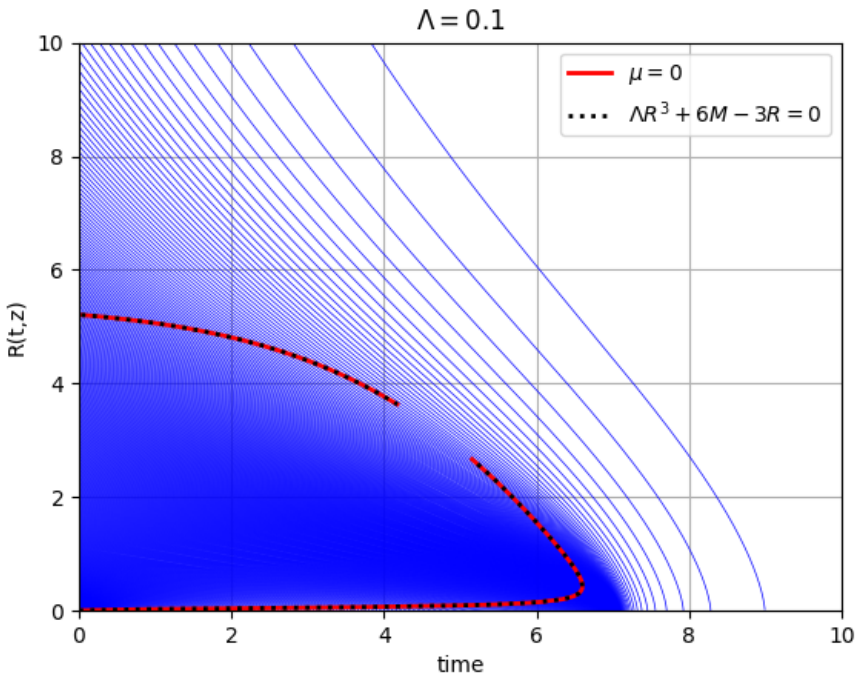

Figure 5.15: Galactic black hole formation, there are two horizons initially that end up merging together after a finite time, and then disappearing. No shell crossings exist for this non-zero Λ model. The gap between the horizons is a result of the initial condition resolution not being fine enough. Fine tuning of the grid of initial conditions is needed to capture a shell moving through certain parts of the horizon at the correct times in these models.

Chapter 6

Conclusion

The Cartan-Karlhede method for determining the equivalence of spacetimes is also an effective tool for invariantly characterizing various physical properties of models in a relativistic framework. The notion of a geometric horizon is an alternative way to characterize black holes in an invariant way which has a lot of utility in the modern day where most systems must be calculated numerically. The numerical efficiency of this method over alternatives such as using scalar polynomial invariants is quite useful when computing much more complicated systems. The Cartan invariants derived here are more simple from a computational standpoint than the SPI analogues. From a Szekeres model perspective, these scalar invariants are simple enough to show a correspondence between the apparent and geometric horizons. A future development of this method for locating horizons may prove useful in modern gravitational wave research, where locating horizons is a paramount concern. Previous work in showcasing this method for utilizing geometric horizons has been done for a plethora of models with exact solutions.

The Szekeres spacetime provides an effective model for formation of galactic black holes, as the Cartan invariants that detect shell crossings can be used as a diagnostic to determine when the models are appropriate. Similarly, the shell crossing detectors are also effective for developing primordial black hole models to determine when these models are valid in the astrophysical context, in the early universe. The physics of the final stages of collapse of GBH or PBH models may be called in to question considering that these QS Szkeres models ignore pressure, which may not necessarily be a good assumption for either of these cases. Future work in the generalized Szekeres-Szafron models that include pressure may be worth studying when it comes to PBH and GBH formation, to get a fuller analysis on the physical aspects of the models. Future work in the generalized Szekeres models with non-vanishing pressure is being considered for the formation of primordial black holes.

Appendix

Derivation of the Field Equations for the Szekeres metric

We can construct the field equations for a dust source with non-zero cosmological constant as follows

The non-zero Einstein Tensor components corresponding to this metric are

$$\begin{aligned} G_{00} &= \frac{R_t^2 R_r + 2R_{rt}RR_t + R_r K}{R^2 R_r} \\ G_{11} &= \frac{R_r^2(2RR_{tt} + R_t^2 + K)}{(K-1)R^2} \\ G_{22} &= -R\frac{2R_{t,r,t}R + 2R_{t,t}R_r + 2R_{r,t}R_t + K_r}{2R_r} \\ G_{33} &= G_{22} \end{aligned} \tag{6.1}$$

The subscript notation here corresponds to partial derivatives with respect to the respective variable. With a dust source, the stress-energy tensor T_{ab} is given by

$$T_{00} = \rho \tag{6.2}$$

where ρ is the energy density of the dust fluid. Using this model, the Einstein field equations (1.1) can be constructed for this spacetime

$$\begin{aligned} G_{00} + \Lambda g_{00} &= 8\pi\rho \\ G_{ii} + \Lambda g_{ii} &= 0 \end{aligned} \tag{6.3}$$

where $i = 1, 2, 3$

For the first equation in (6.3), the field equation becomes

$$\begin{aligned} \frac{R_t^2 R_r + 2R_{rt}RR_t + KR_r + K_r R}{R^2 R_r} - \Lambda &= 8\pi\rho \\ R_t^2 R_r + 2R_{rt}RR_t + KR_r + K_r R - \Lambda R^2 R_r &= 8\pi\rho R^2 R_r \\ (R_t^2 R)_r + (KR)_r - \left(\frac{\Lambda R^3}{3}\right)_r &= 8\pi\rho R^2 R_r \end{aligned} \tag{6.4}$$

The first field equation then can be written as

$$\left(R_t^2 R + KR - \frac{\Lambda R^3}{3}\right)_r = 8\pi\rho R^2 R_r \tag{6.5}$$

From the second equation in (6.3), take the $a = 1$ case

$$G_{11} + \Lambda g_{11} = 0 \tag{6.6}$$

$$\begin{aligned} \frac{R_r^2(2RR_{tt} + R_t^2 + K)}{(K-1)R^2} + \frac{\Lambda R_r^2}{1-K} &= 0 \\ 2RR_{tt} + R_t^2 + K - \Lambda R^2 &= 0 \end{aligned} \tag{6.7}$$

Multiplying both sides of (6.7) by R_t and integrating gives

$$\begin{aligned} 2RR_tR_{tt} + R_t^3 + KR_t - \Lambda R^2 R_t &= 0 \\ \left(R_t^2 R + KR - \frac{\Lambda R^2}{3}\right)_t &= 0 \end{aligned} \tag{6.8}$$

From this we get a first integral to the second field equation

$$R_t^2 R + KR - \frac{\Lambda R^2}{3} = 2M \tag{6.9}$$

Where $M(r)$ is an arbitrary function of integration, and the particular form is chosen to be similar to the mass function in the spacetime. This term is analogous to the mass of a shell of matter with radius r. Using (6.9) to simplify (6.5), the field equations are thus

$$\begin{aligned} 2M_r &= 8\pi\rho R^2 R_r \\ R_t^2 &= \frac{2M(r)}{R} - K(r) + \frac{\Lambda R^2}{3} \end{aligned} \tag{6.10}$$

Curvature Scalars for the QS Szekeres Solution

The forms of these scalars is left in terms of R, H, K so that these terms can fit on the page.

$$\mu = -\frac{1}{2}\frac{\sqrt{2}\left(R_{,t} + \sqrt{1-K\left(r\right)}\right)}{R} \tag{6.11}$$

$$\rho = \frac{1}{2}\frac{\sqrt{2}\left(R_{,t} - \sqrt{1-K\left(r\right)}\right)}{R} \tag{6.12}$$

$$\tau = \frac{\left(-\left(\frac{\partial^2}{\partial x \partial r}H\right)H - i\left(\frac{\partial^2}{\partial y \partial r}H\right)H + \left(i\frac{\partial}{\partial y}H + \frac{\partial}{\partial x}H\right)\frac{\partial}{\partial r}H\right)\sqrt{2}}{4\,R\frac{\partial}{\partial r}H - 4\left(\frac{\partial}{\partial r}R\right)H} \tag{6.13}$$

$$\kappa = -\frac{\left(-\left(\frac{\partial^2}{\partial x \partial r}H\right)H - i\left(\frac{\partial^2}{\partial y \partial r}H\right)H + \left(i\frac{\partial}{\partial y}H + \frac{\partial}{\partial x}H\right)\frac{\partial}{\partial r}H\right)\sqrt{2}}{4\,R\frac{\partial}{\partial r}H - 4\left(\frac{\partial}{\partial r}R\right)H} \tag{6.14}$$

$$\gamma = \frac{\left(\left(\frac{\partial}{\partial t}R\right)\frac{\partial}{\partial r}H - \left(\frac{\partial^2}{\partial t \partial r}R\right)H\right)\sqrt{2}}{4\,R\frac{\partial}{\partial r}H - 4\left(\frac{\partial}{\partial r}R\right)H} \tag{6.15}$$

$$\lambda = 0 \tag{6.16}$$

$$\alpha = \frac{-i/4\left(i\frac{\partial}{\partial x}H + \frac{\partial}{\partial y}H\right)\sqrt{2}}{R} \tag{6.17}$$

$$\epsilon = \frac{\left(\left(\frac{\partial^2}{\partial t \partial r}R\right)H - \left(\frac{\partial}{\partial t}R\right)\frac{\partial}{\partial r}H\right)\sqrt{2}}{4\,R\frac{\partial}{\partial r}H - 4\left(\frac{\partial}{\partial r}R\right)H} \tag{6.18}$$

$$\beta = \frac{i/4\left(i\frac{\partial}{\partial x}H - \frac{\partial}{\partial y}H\right)\sqrt{2}}{R} \tag{6.19}$$

$$\sigma = 0 \tag{6.20}$$

$$\nu = -\frac{\left(\left(\frac{\partial^2}{\partial x \partial r}H\right)H - i\left(\frac{\partial^2}{\partial y \partial r}H\right)H + \left(i\frac{\partial}{\partial y}H - \frac{\partial}{\partial x}H\right)\frac{\partial}{\partial r}H\right)\sqrt{2}}{4\,R\frac{\partial}{\partial r}H - 4\left(\frac{\partial}{\partial r}R\right)H} \tag{6.21}$$

$$\pi = \frac{\left(\left(\frac{\partial^2}{\partial x \partial r}H\right)H - i\left(\frac{\partial^2}{\partial y \partial r}H\right)H + \left(i\frac{\partial}{\partial y}H - \frac{\partial}{\partial x}H\right)\frac{\partial}{\partial r}H\right)\sqrt{2}}{4\,R\frac{\partial}{\partial r}H - 4\left(\frac{\partial}{\partial r}R\right)H} \tag{6.22}$$

Bibliography

[1] Abhay Ashtekar and Badri Krishnan. Dynamical horizons: Energy, angular momentum, fluxes, and balance laws. *Physical Review Letters*, 89(26), Dec 2002.

[2] Abhay Ashtekar and Badri Krishnan. Isolated and dynamical horizons and their applications. *Living Reviews in Relativity*, 7(1), Dec 2004.

[3] Ivan Booth. Black-hole boundaries. *Canadian Journal of Physics*, 83(11):1073–1099, Nov 2005.

[4] Robert G. Buckley and Eric M. Schlegel. Physical geometry of the quasispherical szekeres models. *Physical Review D*, 101(2), Jan 2020.

[5] A.A. Coley, N. Layden, and D.D. McNutt. An invariant characterization of the quasi-spherical Szekeres dust models. *General Relativity and Gravitation*, 51(12):164, 2019.

[6] Alan A. Coley, David D. McNutt, and Andrey A. Shoom. Geometric horizons. *Physics Letters B*, 771:131–135, Aug 2017.

[7] Ujjal Debnath, Soma Nath, and Subenoy Chakraborty. Quasi-spherical collapse with cosmological constant. *Monthly Notices of the Royal Astronomical Society*, 369(4):1961–1964, July 2006.

[8] J.R. Dormand and P.J. Prince. A family of embedded runge-kutta formulae. *Journal of Computational and Applied Mathematics*, 6(1):19 – 26, 1980.

[9] Carl Eckart. The thermodynamics of irreversible processes. iii. relativistic theory of the simple fluid. *Physical Review*, 58:919–924, Nov 1940.

[10] Albert Einstein. Die Feldgleichungen der Gravitation. (German) [The field equations of gravitation]. *Koniglich Preussische Akademie der Wissenschafen*, pages 844–847, 1915.

[11] Tomohiro Harada and Sanjay Jhingan. Spherical and nonspherical models of primordial black hole formation: exact solutions. *Progress of Theoretical and Experimental Physics*, 2016(9):093E04, Sep 2016.

[12] S. W. Hawking and G. F. R. Ellis. *The Large Scale Structure of Space-Time*. Cambridge Monographs on Mathematical Physics. Cambridge University Press, 1973.

[13] S.W. Hawking and R. Penrose. The Singularities of gravitational collapse and cosmology. *Proceedings of the Royal Soceity of London A*, A314:529–548, 1970.

[14] Charles Hellaby. The nonsimultaneous nature of the schwarzschild r=0 singularity. *Journal of Mathematical Physics*, 37(6):2892–2905, 1996.

[15] Charles Hellaby and Andrzej Krasiński. You cannot get through szekeres wormholes: Regularity, topology, and causality in quasispherical szekeres models. *Physical Review D*, 66(8), Oct 2002.

[16] Andrzej Krasiński and Krzysztof Bolejko. Apparent horizons in the quasispherical szekeres models. *Physical Review D*, 85(12), June 2012.

[17] Nicholas Layden. https://github.com/nicklayden/blazar.

[18] Waterloo Ontario. Maple 2018. Maplesoft, a division of Waterloo Maple Inc.

[19] D. D. McNutt, M. A. H. MacCallum, D. Gregoris, A. Forget, A. A. Coley, P. C. Chavy-Waddy, and D. Brooks. Cartan invariants and event horizon detection, extended version, 2017.

[20] Ezra Newman and Roger Penrose. An approach to gravitational radiation by a method of spin coefficients. *Journal of Mathematical Physics*, 3(3):566–578, 1962.

[21] Boost Organization. Boost c++ libraries. 1998-2020.

[22] K. Schwarzschild. On the gravitational field of a mass point according to Einstein's theory. *arXiv e-prints*, page physics/9905030, May 1999.

[23] Hans Stephani, Dietrich Kramer, Malcolm MacCallum, Cornelius Hoenselaers, and Eduard Herlt. *Exact Solutions of Einstein's Field Equations*. Cambridge Monographs on Mathematical Physics. Cambridge University Press, 2 edition, 2003.

[24] Roberto A Sussman and Krzysztof Bolejko. A novel approach to the dynamics of szekeres dust models. *Classical and Quantum Gravity*, 29(6):065018, March 2012.

[25] P. Szekeres. A class of inhomogeneous cosmological models. *Communications in Mathematical Physics*, 41(1):55–64, February 1975.